Spectra of Diffusion, Dispersion, and Dissipation for Kinetic Alfvénic and Compressive Turbulence: Comparison between Kinetic Theory and Measurements from MMS

Jiansen He[1] , Xingyu Zhu[1] , Daniel Verscharen[2,3] , Die Duan[1] , Jinsong Zhao[4] , and Tieyan Wang[5]

[1] School of Earth and Space Sciences, Peking University, Beijing 100871, Beijing, People's Republic of China; jshept@pku.edu.cn
[2] Mullard Space Science Laboratory, University College London, Dorking RH5 6NT, UK
[3] Space Science Center, University of New Hampshire, Durham, NH 03824, USA
[4] Key Laboratory of Planetary Sciences, Purple Mountain Observatory, Chinese Academy of Sciences, Nanjing 210008, People's Republic of China
[5] RAL Space, STFC, Oxfordshire, OX11 0QX, UK

Abstract

We analyze measurements from Magnetospheric Multiscale mission to provide the spectra related with diffusion, dispersion, and dissipation, all of which are compared with predictions from plasma theory. This work is one example of magnetosheath turbulence, which is complex and diverse and includes more wave modes than the kinetic Alfvénic wave (KAW) mode studied here. The counter-propagation of KAW is identified from the polarities of cross-correlation spectra: $CC(N_e, |B|)$, $CC(V_{e\perp}, B_\perp)$, $CC(V_{e\parallel}, B_\parallel)$, and $CC(N_e, V_{e\parallel})$. We propose the concepts of turbulence ion and electron diffusion ranges (T-IDRs and T-EDRs) and identify them practically based on the ratio between electric field power spectral densities in different reference frames: $PSD(\delta E'_{i,local})/PSD(\delta E_{global})$ and $PSD(\delta E'_{e,local})/PSD(\delta E_{global})$. The outer scales of the T-IDR and T-EDR are observed to be at the wavenumber of $kd_i \sim 0.2$ and $kd_e \sim 0.1$, where d_i and d_e are the proton and electron inertial lengths, respectively. The signatures of positive dispersion related to the Hall effect are illustrated observationally and reproduced theoretically with flat $PSD(\delta E_{global})$ and steep $PSD(\delta B)$, as well as a bifurcation between $PSD(\delta V_i)$ and $PSD(\delta V_e)$. We calculate the dissipation rate spectra, $\gamma(k)$, which clearly show the commencement of dissipation around $kd_i \sim 1$. We find that the dissipation in this case is mainly converted to electron parallel kinetic energy, responsible for the electron thermal anisotropy with $T_{e,\parallel}/T_{e,\perp} > 1$. The "3D" (diffusion, dispersion, and dissipation) characteristics of kinetic Alfvénic and compressive plasma turbulence are therefore summarized as follows: positive dispersion due to the Hall effect appears in the T-IDR, while dominant parallel dissipation with energy transferred to electrons occurs mainly in the T-EDR.

1. Introduction

Space plasma turbulence consists of fluctuations at scales ranging from magnetohydrodynamic (MHD) to kinetic scales (Bruno & Carbone 2013; Kiyani et al. 2015; Wu et al. 2016). The power spectral density of turbulent fluctuations, e.g., in δB, exhibits a break between two power-law sections near the ion kinetic scale, clearly indicating the difference between MHD and kinetic physics in turbulence (Alexandrova et al. 2009; Sahraoui et al. 2009; Huang et al. 2014). The location of the spectral break, a scale indicating the onset of additional kinetic effects, is an important quantity. Its dependence on the ion thermal gyroradius and/or ion inertial length is a topic that has been intensively studied (Perri et al. 2010; Bourouaine et al. 2012; Smith et al. 2012; Bruno & Trenchi 2014; Chen et al. 2014a; Cerri et al. 2016; Franci et al. 2016; Duan et al. 2018; Wang et al. 2018; Woodham et al. 2018).

It was predicted and found that ions and electrons successively become unfrozen/diffusive with respect to the magnetic field when gradually approaching the core region of magnetic reconnection, which is characterized by regions of large changes in the magnetic topology (Birn & Priest 2007). The physics of the ion diffusion region has been studied thoroughly by means of Hall-MHD and hybrid (ion kinetic + electron fluid) simulations (Birn et al. 2001; Ma & Bhattacharjee 2001), and observed fRequently by the Cluster satellites (Deng & Matsumoto 2001; Mozer et al. 2002; He et al. 2008; Zhou et al. 2009; Fu et al. 2016). The electron kinetics in the electron

diffusion region as one of the thus far major unresolved puzzles in reconnection physics has been investigated intensively via fully kinetic particle-in-cell simulations (Pritchett 2001; Lu et al. 2010), and studied observationally thanks to the high-quality data of electrons and electromagnetic fields from the Magnetospheric Multiscale (MMS) satellites (Burch et al. 2016b; Li et al. 2016; Tang et al. 2019; Phan et al. 2018). The spatial inhomogeneity created by the ion and electron diffusion regions of magnetic reconnection is usually treated as an isolated object, i.e., a structure with a localized spatial gradient distinguishable from the background. For a turbulent environment filled with spatial inhomogeneities, it is still unclear how to identify and characterize the ion and electron diffusion phenomena, which is a newly emerging topic evoking the attention and interest of researchers.

Dispersion (i.e., the scale dependence of phase speed) is another characteristic appearing in the kinetic range. In contrast, the three types of MHD waves are nondispersive. According to the theory of waves in plasmas (see, for example, the textbooks by Stix 1992; Gary 1993), Alfvén waves at kinetic scales propagating at different angles show two distinct dispersion relations: negative (i.e., $\frac{\partial^2 \omega}{\partial k^2} < 0$) and positive dispersion (i.e., $\frac{\partial^2 \omega}{\partial k^2} > 0$) for parallel propagating ion-cyclotron waves and quasi-perpendicular kinetic Alfvén waves, respectively. Such different characteristics of dispersion relations have been applied to diagnose the wave modes in space plasmas (e.g., Narita et al. 2011; He et al. 2013; Roberts et al. 2015; Zhao 2015; Zhao et al. 2019b). The k-filtering/wave-telescope tool has been successfully employed to

measurements from Cluster and MMS to reconstruct the dispersion relation in frequency-wavenumber space (Sahraoui et al. 2010; Narita et al. 2011; Roberts et al. 2015; Narita et al. 2016). This method and other studies reveal the complex nature of turbulence at kinetic scales: oblique kinetic Alfvén waves and/or convected coherent structures can be responsible for the low-frequency fluctuations in the plasma frame (Sahraoui et al. 2010; Roberts et al. 2015); whistler waves can account for the fluctuations at higher frequencies (Narita et al. 2011); and the compressive fluctuations propagating obliquely at about 60° can be interpreted as kinetic-drift mirror modes (Narita et al. 2016).

The ratio of PSDs between electric and magnetic fields, a proxy for the squared phase speed, is found to increase approximately quadratically with increasing spacecraft-frame frequency around the ion scales (Bale et al. 2005; Salem et al. 2012; Chen & Boldyrev 2017; Matteini et al. 2017; Zhu et al. 2019). The main reason for this dispersive behavior in the kinetic range lies in the decoupling between proton and electron species in terms of their magnetization behavior. For example, the quadratic behavior of the frequency with increasing wavenumber for quasi-parallel propagating whistler waves and quasi-perpendicular propagating kinetic Alfvén waves is mainly related to the difference of transverse velocity between protons and electrons. To really understand the physics underneath this dispersion phenomenon, one needs to investigate the difference between $PSD(\delta V_i)$ and $PSD(\delta V_e)$.

Dissipation as a sink for cascaded energy in turbulence is also an important and unique process at kinetic scales (Tu & Marsch 1995; Cranmer & van Ballegooijen 2012; Matthaeus et al. 2015). It is hypothesized that the cascaded turbulence gradually deposits its energy into the plasma as the length scales of the fluctuations decrease (Howes et al. 2008; Yang et al. 2019). There are various candidates of energy conversion channels for the turbulence dissipation: Landau resonance belonging to the category of wave–particle interactions, cyclotron resonance pertaining to wave–particle interactions as well, non-resonant scattering and stochastic heating of particles by turbulent fields, dissipation of intermittent current structures via processes like magnetic reconnection, etc. (Chandran et al. 2010; Cranmer et al. 2015; He et al. 2015b, 2015c, 2019a, 2019b; Howes et al. 2017; Klein et al. 2017; Chasapis et al. 2018; Chen et al. 2019). In space plasma physics, the dominance of these dissipation mechanisms is a matter of ongoing debate. In principle, the overall dissipation process is unlikely to be exclusive to an individual mechanism in a complicated space plasma system. Different dissipation mechanisms may be applicable to and responsible for the plasma energization in different situations.

In this work, we investigate the diffusion, dispersion, and dissipation of compressive kinetic turbulence by employing newly developed methods to analyze the measurements of magnetosheath turbulence from the MMS spacecraft. We focus our detailed study on measurement intervals in the magnetosheath during which kinetic Alfvénic wave (KAWs) are present. This mode is one of the prominent candidates for the plasma fluctuations at kinetic scales (Schekochihin et al. 2009; He et al. 2012; Chen et al. 2013; Šafránková et al. 2013; Roberts et al. 2018; Wu et al. 2019). We note, however, that our work does not quantify the statistical occurrence of KAWs compared to the statistical occurrence of other modes and other forms of turbulence in the magnetosheath. Such a quantification lies beyond the scope of this work. The paper begins with

an overview of magnetosheath turbulence measurements in Section 2. The wave nature of the turbulence is elucidated in Section 3. The evidence for positive dispersion due to the Hall effect is provided in Section 4. Measures of ion and electron diffusion as functions of scale are introduced in Section 5. The dissipation rate spectra in different directions with respect to the background magnetic field and for different species are illustrated in Section 6. A summary and discussion are provided in the final section.

2. Overview of Measurements in Magnetosheath Turbulence

To fulfill the goal of studying comprehensively the "3D" (diffusion, dispersion, and dissipation) characteristics of kinetic turbulence, we choose a case of burst-mode measurements with high-cadence sampling of all variables when MMS was in the magnetosheath during [08:58, 09:08] on 2016 December 9. The measurement data analyzed here are from the FPI and FIELDS instruments on board MMS (Burch et al. 2016a; Pollock et al. 2016; Torbert et al. 2016).

Time sequences of observable quantities are plotted in Figure 1 to show the basic features of the magnetosheath turbulence during this time interval. According to Figure 1(a), both plasma electron density (N_e) and magnetic field strength ($|\boldsymbol{B}|$) are highly oscillating rather than quasi-static, with the ratio of maximum to minimum values being as large as 3. When comparing carefully the fluctuation trends between N_e and $|\boldsymbol{B}|$ throughout the time interval, we find: (1) δN_e and $\delta|\boldsymbol{B}|$ are mostly positively correlated in the first half of the interval, (2) yet they are more anticorrelated in the second half of the interval. The three components (x, y, z in GSE coordinates) of ion bulk velocity, electron bulk velocity, and magnetic field vectors are displayed in Figures 1(b), (c), and (d). The time sequences of $\boldsymbol{V}_i$ can be viewed as a proxy of smoothed $\boldsymbol{V}_e$, the latter of which has rapid, large-amplitude oscillation at higher frequency. Anticorrelation between ($\boldsymbol{V}_i$, $\boldsymbol{V}_e$) and $\boldsymbol{B}$ can also be identified from the time profiles. The parallel and perpendicular temperatures of protons and electrons are displayed in Figures 1(e) and (f). The protons are thermally isotropic almost all the time although the proton temperature varies with time frequently and by a large amount. In contrast, the electrons exhibit remarkable thermal anisotropy with $T_{e\parallel} > T_{e\perp}$ at most times. The plasma thermal states suggest the existence of a parallel heating process for electrons underlying the observations. The energy source for electron heating is believed to come from the dissipation of kinetic turbulence, which will be discussed in later sections.

3. Compressibility and Alfvénicity of Wave-like Turbulence at Kinetic Scales

In this section, we study the nature of turbulence by checking whether it is wave-like, with its quantities varying in a certain polarization relationship, or just random fluctuations, without connection between its quantities. Our technique of spectral correlation that was proposed by He et al. (2015a) is applied to different pairs of variables: (N_e, $|\boldsymbol{B}|$), ($V_{e\perp1}$, $B_{\perp1}$), ($V_{e\perp2}$, $B_{\perp2}$), ($V_{e\parallel}$, $B_{\parallel}$), and (N_e, $V_{e\parallel}$). Before the spectral correlation analysis, the magnetic and velocity vectors are transformed from the GSE coordinates to the local background field-aligned coordinates (LB-FAC). The three directions ($\boldsymbol{e}_\parallel$, $\boldsymbol{e}_{\perp1}$, and $\boldsymbol{e}_{\perp2}$) associated with LB-FAC are obtained as
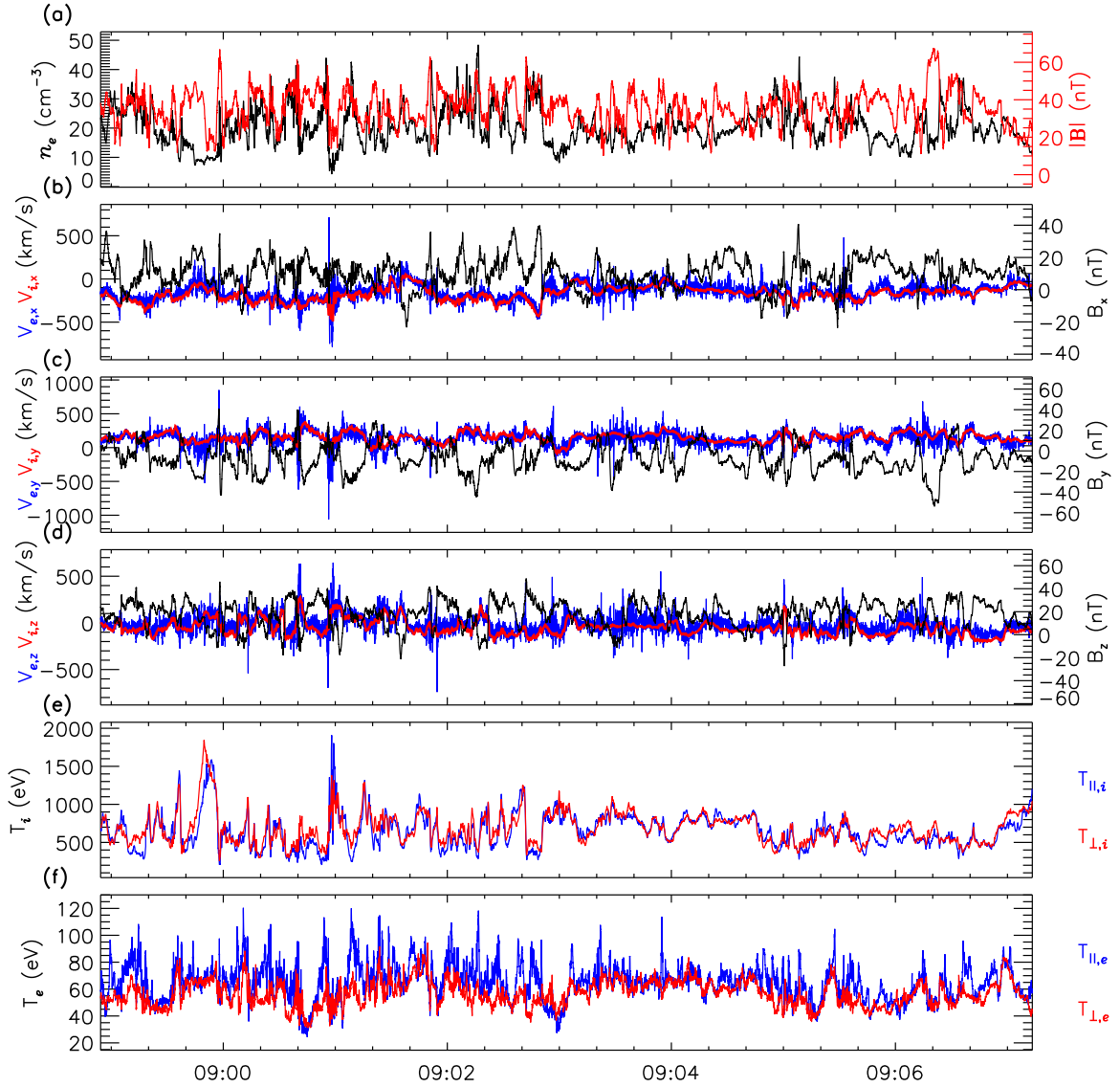
Figure 1. Time sequences of variables (N_e, $|\boldsymbol{B}|$, $\boldsymbol{B}$, $\boldsymbol{V}_e$, $\boldsymbol{V}_i$, T_i, and T_e) observed by MMS-1 during [08:58, 09:08] on 2016 December 9.

follows: (1) we conduct a convolution of the magnetic vector sequence with Gaussian functions of various scales to determine the local background magnetic vector and the corresponding direction $\boldsymbol{e}_{\parallel}$ (Horbury et al. 2008; Podesta 2009); (2) we calculate the direction $\boldsymbol{e}_{\perp 1}$ as the cross product of $\boldsymbol{e}_{\parallel}$ and $\boldsymbol{V}_{\mathrm{BulkFlow}}$; and (3) we calculate $\boldsymbol{e}_{\perp 2}$ to complete the right-handed system. In Figure 2, we plot spectrograms of cross-correlation between two fluctuating variables, e.g., CC(A, B) for variables A and B. According to Figure 2(a), CC(N_e, $|\boldsymbol{B}|$) is mainly negative throughout the time interval below the period of 1 s, while it is both positive and negative in the first and second half of the time interval at periods larger than 1 s. The correlation CC($B_{\perp 1}$, $V_{\perp 1}$) is dominant with negative values at periods larger than 1 s, while it tends to be more alternating between positive and negative values at periods less than 1 s (see Figure 2(b)). In Figure 2(c), CC($B_{\perp 2}$, $V_{\perp 2}$) displays a distribution similar to that of CC($B_{\perp 1}$, $V_{\perp 1}$). It is also interesting to note the prevalence of opposite polarities between CC($B_{\parallel}$, $V_{e\parallel}$) and CC(N_e, $V_{e\parallel}$) at many times throughout the period range by comparing Figures 2(d) and (e). The aforementioned polarization analyses show that the turbulence

is significantly more complex than a superposition of individual turbulent wave modes: (1) composition of the fast magnetosonic, slow magnetosonic, and Alfvénic waves in the MHD range; (2) possible coexistence of counter-propagating kinetic Alfvénic waves and kinetic slow-mode waves in the kinetic range.

Figure 3 shows evidence of counter-propagating compressive Alfvénic waves at kinetic scales, the signals of which are obtained from wavelet decomposition of the fluctuations at small scales around 0.7 s. The wavelet decomposition approach, which serves as a bandpass filter, had been successfully applied to identify the magnetic polarization of ion-cyclotron waves and kinetic Alfvén waves (He et al. 2012), as well as coherent events (Lion et al. 2016) in solar wind turbulence. The left and right columns of Figure 3 display the correlated or anticorrelated variables: CC(δN_e, $\delta|\boldsymbol{B}|$) < 0, CC($\delta V_{e\perp 1}$, $\delta B_{\perp 1}$) < 0, CC($\delta V_{e\perp 2}$, $\delta B_{\perp 2}$) < 0, CC($\delta V_{e\parallel}$, $\delta B_{\parallel}$) < 0, and CC($\delta V_{e\parallel}$, δn_e) > 0 on the left side for the correlation of kinetic waves with $\boldsymbol{k} \cdot \boldsymbol{B}_0 > 0$; (2) CC($\delta N_e$, $\delta|\boldsymbol{B}|$) < 0, CC($\delta V_{e\perp 1}$, $\delta B_{\perp 1}$) > 0, CC($\delta V_{e\perp 2}$, $\delta B_{\perp 2}$) > 0, CC($\delta V_{e\parallel}$, $\delta B_{\parallel}$) > 0, and CC($\delta V_{e\parallel}$, δn_e) < 0 on the right side for the correlation of kinetic waves with $\boldsymbol{k} \cdot \boldsymbol{B}_0 < 0$.
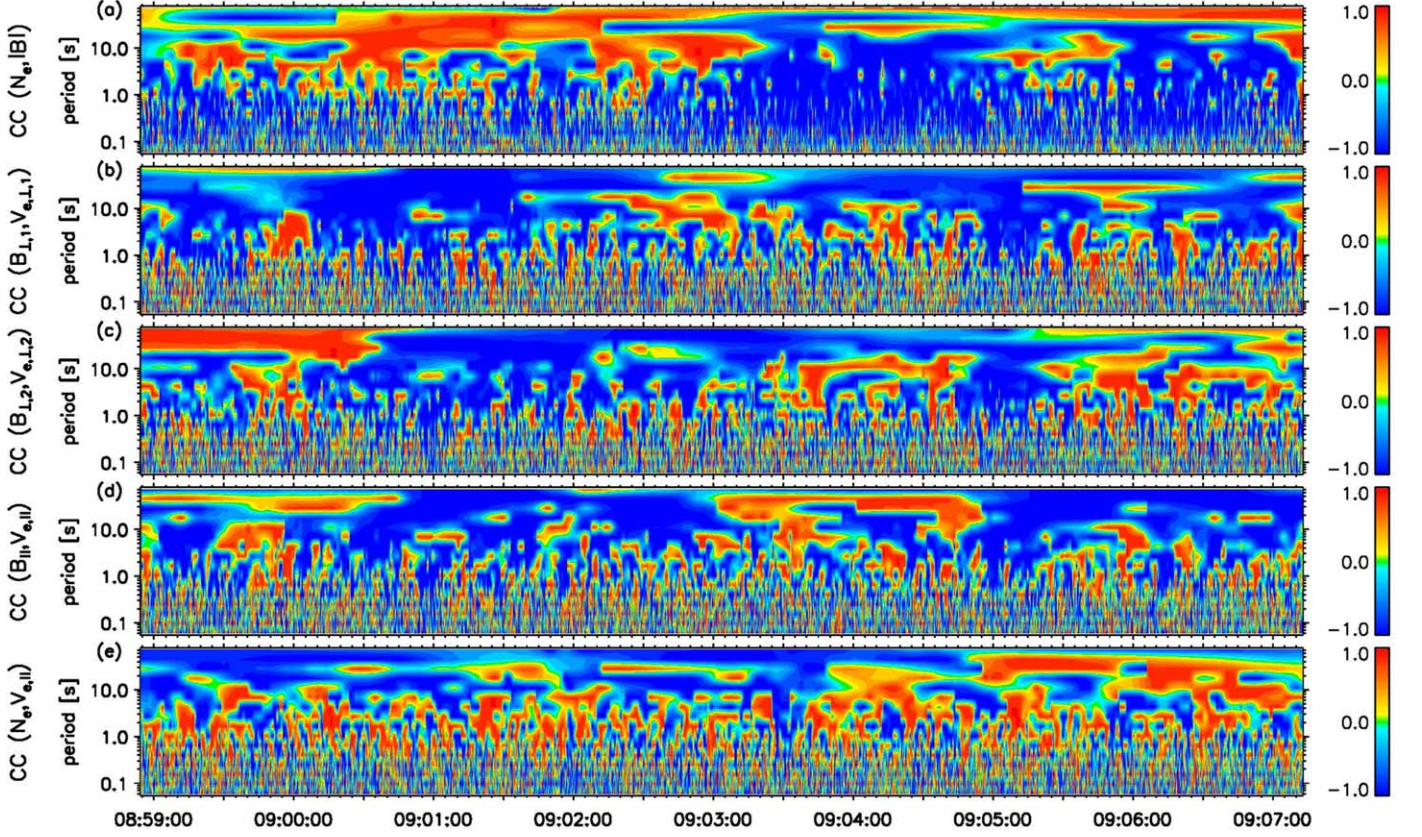
Figure 2. Cross-correlation spectra of different pairs of variables: CC(N_e, $|\boldsymbol{B}|$), CC($B_{\perp 1}$, $V_{e\perp 1}$), CC($B_{\perp 2}$, $V_{e\perp 2}$), CC($B_\parallel$, $V_{e\parallel}$), and CC(N_e, $V_{e\parallel}$).

4. Dispersion Signature of Kinetic Alfvénic and Compressive Turbulence

Based on Faraday's law, the ratio of electric field and magnetic field power spectral densities is often invoked to analyze the dispersion relation, and to successfully identify KAWs in the kinetic and inertial regimes in the solar wind and in the polar geo-magnetosphere, respectively (Bale et al. 2005; Salem et al. 2012; Chen et al. 2014b). The flattening of the PSD (δE) spectrum, while the PSD(δB) spectrum steepens, is a consequence of the Hall effect, which itself is the result of the decoupling between the ion motion and the electron motion at scales of the order of and smaller than the proton inertial length. In previous studies, almost exclusively the PSDs for the perpendicular components of electric and magnetic field vectors were used to estimate the dispersion relation. Here, we plot a comprehensive set of PSDs in Figure 4, taking into account the measurable/accessible variables as completely as possible: (1) PSDs for the trace, parallel component, perpendicular component, and magnitude of δB; (2) PSDs for the trace, parallel and perpendicular components of $\delta \boldsymbol{E}_{\text{i,global}} = \boldsymbol{E}_{\text{SC}} + \langle \boldsymbol{V}_i \rangle \times \boldsymbol{B}$, where $\delta \boldsymbol{E}_{\text{i,global}}$ and $\boldsymbol{E}_{\text{SC}}$ represent, respectively, the electric fields in the reference frames of ion global/mean bulk flow and the MMS spacecraft; (3) PSDs for $\boldsymbol{E}_{\text{SC}}$, $\delta \boldsymbol{E}'_{\text{i,loc}}$ ($= \boldsymbol{E}_{\text{SC}} + \boldsymbol{V}_i \times \boldsymbol{B}$), and $\delta \boldsymbol{E}'_{\text{e,loc}}$ ($= \boldsymbol{E}_{\text{SC}} + \boldsymbol{V}_e \times \boldsymbol{B}$), where $\delta \boldsymbol{E}'_{\text{i,loc}}$ and $\delta \boldsymbol{E}'_{\text{e,loc}}$ represent, respectively, the electric fields in the reference frames of ion and electron local bulk flows; (4) PSDs for δN_e, δV_e, and δV_i; (5) PSDs for the current density, $\boldsymbol{J}_{\text{plasma}} = n_e q(\boldsymbol{V}_i - \boldsymbol{V}_e)$ based on the moments of particles and $\boldsymbol{J}_{\text{CurlB}} = \nabla \times \boldsymbol{B}/\mu_0$ based on the curlometer technique.

It can be seen in Figure 4(a) that the magnetic field is highly compressive, with PSD($\delta B_\parallel$) being comparable to or even larger than PSD($\delta B_\perp$), over the SC-frame frequency range of [0.01, 10] Hz. Therefore, the branch of Alfvén waves and kinetic Alfvén waves may not be fully responsible for the observed compressive behavior. Two breaks with a transition to a steeper profile at larger frequency can be discerned around $f_{\text{SC}} \sim 0.1$ Hz and $f_{\text{SC}} \sim 2$ Hz on the magnetic PSD profiles. The break frequency $f_{\text{SC}} \sim 0.1$ Hz corresponds to the correlation timescale. We therefore identify it with the outer scale of turbulence cascade ($f_{\text{outer-scale}} \sim 0.1$ Hz). The turbulence energy contained in the frequency range with $f < f_{\text{outer-scale}}$ is injected into the cascade in the inertial range $f > f_{\text{outer-scale}}$, which, to be more precise, is the "ion-kinetic inertial range" rather than the "MHD inertial range" since $f > f_{\text{outer-scale}}$ corresponds to $kd_i > 0.1$. In addition to the connection to the correlation scale, another reason to identify $kd_i > 0.1$ (on the right of the first break) as "ion-kinetic inertial range" rather than "ion kinetic dissipation range" comes from the fact that the dissipation rate spectrum stays at a level near zero in this range, which will be presented in a later section. The second break occurs at $f_{\text{SC}} \sim 2$ Hz corresponding to $kd_i \sim 2$ or $kd_e \sim 0.05$, indicating a possible separation between ion and electron kinetic ranges. We will find in the following section that the dissipation rate spectrum increases beyond $kd_i \sim 2$ ($kd_e \sim 0.05$), manifesting the existence of an "electron-kinetic dissipation range."

Figure 4(b) displays the PSDs for the trace, parallel, and perpendicular components of electric field fluctuations in the reference frame of the global/mean ion bulk flow, $\delta E = \boldsymbol{E}_{\text{SC}} + \langle \boldsymbol{V}_i \rangle \times \boldsymbol{B}$. A shallower tail of PSD(δE_{trace}), with
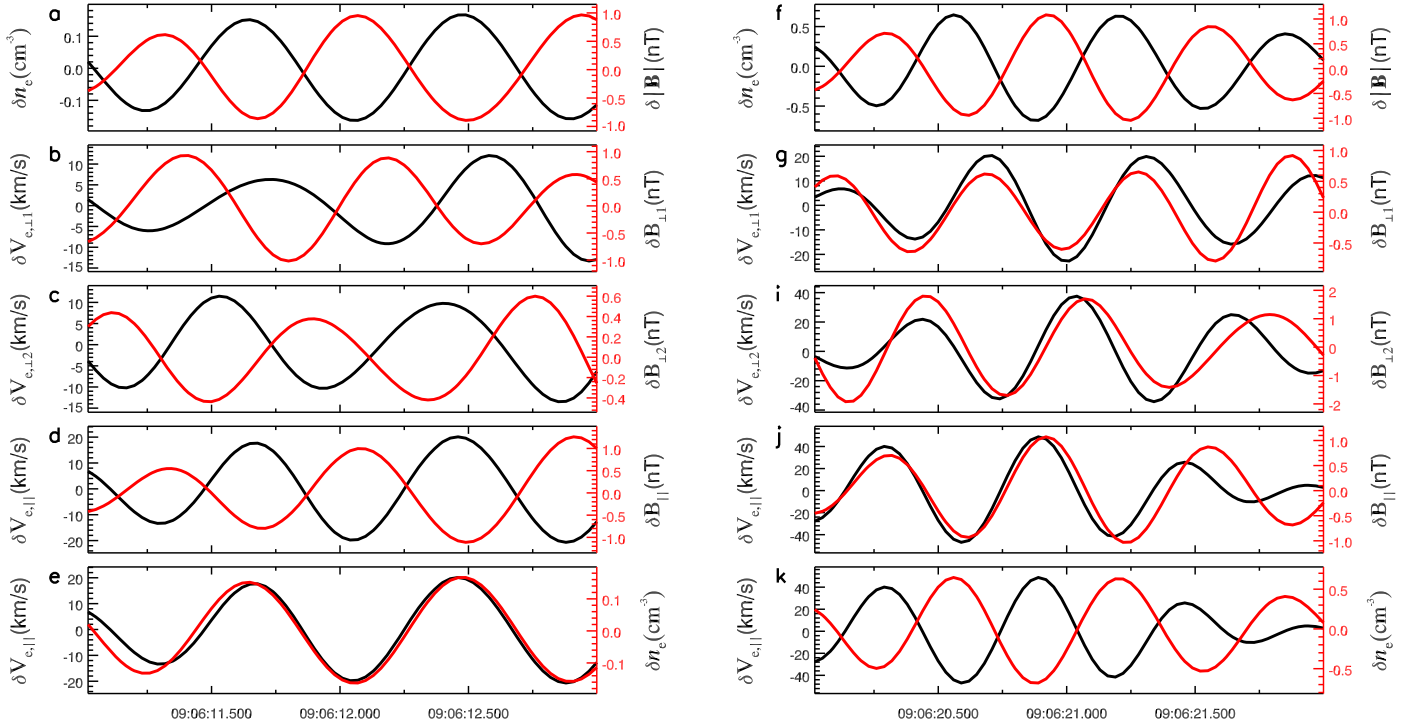
Figure 3. Examples of counter-propagating compressible kinetic Alfvénic waves with $\mathbf{k} \cdot \mathbf{B}_0 > 0$ on the left and $\mathbf{k} \cdot \mathbf{B}_0 < 0$ on the right. Sub-bands of δN_e, $\delta|\mathbf{B}|$, $\delta B_{\perp 1}$, $\delta B_{\perp 2}$, $\delta B_{\parallel}$, $\delta V_{e\perp 1}$, $\delta V_{e\perp 2}$, and $\delta V_{e\parallel}$ at periods around 0.7 s, as extracted through wavelet decomposition, are displayed in comparison with each other.

the exception of its high-frequency end, follows the steeper PSD(δE_{trace}) around the conjunction of $f \sim 1$ Hz. PSD($\delta E_\perp$) dominates over PSD($\delta E_\parallel$) throughout the whole frequency range, albeit not as strongly as predicted by quasi-perpendicular Alfvén and kinetic Alfvén waves. PSD(δV_i) and PSD(δV_e) match well with each other at frequencies less than 0.1 Hz, and start to bifurcate at higher frequencies beyond 0.1 Hz (see Figure 4(c)). Above 0.1 Hz, the proton bulk velocity fluctuation (δV_i) decays much more rapidly with increasing frequency than the electron bulk velocity fluctuation (δV_e): PSD($\delta V_i(f)$) $\sim f^{-2.49}$, PSD($\delta V_e(f)$) $\sim f^{-0.96}$. In the small frequency range with $f \in [0.04, 0.1]$ Hz, we obtain the power-law fitting results: PSD($\delta V_i(f)$) $\sim f^{-1.53}$, PSD($\delta V_e(f)$) $\sim f^{-1.51}$. The proton fluid tends to become immobile, leaving only the electron fluid to convect and stir the turbulent magnetic flux beyond ion kinetic scales. The relative compressibility measures, PSD($\delta N_e/N_0$) and PSD($\delta|\mathbf{B}|/B_0$), are comparable or even of equal amplitude with each other throughout the frequency range, the spectral breaks of which look similar to that of PSD(δB_{trace})obs.

In Figure 4(e), the current density spectra PSD($\delta J_{\text{trace,plasma}}$) and PSD($\delta J_{\text{trace,curlB}}$) match with each other, showing a power-law profile of $f_{\text{sc}}^{-0.5}$ until $f_{\text{sc}} \sim 1$ Hz, above which PSD($\delta J_{\text{trace,curlB}}$) drops down dramatically due to the finite spatial separation between the MMS satellites used for the curlometer technique. The power spectra of electric fields in the reference frames of global bulk flow and local bulk flows (PSD($\delta E_{\text{i,global}}$), PSD($\delta E'_{\text{i,local}}$), and PSD($\delta E'_{\text{e,local}}$)) are illustrated in Figure 4(f). PSD($\delta E'_{\text{i,local}}$) and PSD($\delta E'_{\text{e,local}}$) merge with PSD($\delta E_{\text{i,global}}$) at $f_{\text{sc}} \sim 1$ Hz ($kd_i \sim 1$) and $f_{\text{sc}} \sim 10$ Hz ($kd_i \sim 10$, $kd_e \sim 0.23$).

To further examine the nature of kinetic turbulence, we calculate the predictions of PSDs for variables by multiplying PSD($\delta B_\perp$)obs. as the most basic PSD from our observations

with the power ratios from linear KAW theory based on a two-fluid approach, and then compare the predicted PSDs (PSD$_{\text{part obs.} \rightarrow \text{theory}}$) with the pure observations (PSD$_{\text{obs.}}$). The propagation angle used in the linear KAW theory is assumed to be 89° or 91° with respect to the background magnetic field direction. The concrete formulas for PSD(δB_{trace})$_{\text{partobs.} \rightarrow \text{theory}}$, PSD($\delta E_{\text{trace}}$)$_{\text{partobs.} \rightarrow \text{theory}}$, PSD($\delta V_{\text{i,trace}}$)$_{\text{partobs.} \rightarrow \text{theory}}$, PSD($\delta V_{\text{e,trace}}$)$_{\text{partobs.} \rightarrow \text{theory}}$, PSD($\delta N_e/N_0$)$_{\text{partobs.} \rightarrow \text{theory}}$, PSD($\delta|\mathbf{B}|/B_0$)$_{\text{partobs.} \rightarrow \text{theory}}$, PSD($\delta J_{\text{trace}}$)$_{\text{partobs.} \rightarrow \text{theory}}$ are as follows:

$$\text{PSD}(\delta \mathbf{B}_{\text{trace}})_{\text{part obs.} \rightarrow \text{theory}} = \text{PSD}(\delta \mathbf{B}_\perp)_{\text{obs.}}$$
$$\cdot \left(\frac{|\delta \mathbf{B}_{\text{trace}}|^2}{|\delta \mathbf{B}_\perp|^2} \right)_{\text{KAW-theory}}, \quad (1a)$$

$$\text{PSD}(\delta \mathbf{E}_{\text{trace}})_{\text{part obs.} \rightarrow \text{theory}} = \text{PSD}(\delta \mathbf{B}_\perp)_{\text{obs.}}$$
$$\cdot \left(\frac{|\delta \mathbf{E}_{\text{trace}}|^2}{|\delta \mathbf{B}_\perp|^2} \right)_{\text{KAW-theory}}, \quad (1b)$$

$$\text{PSD}(\delta \mathbf{V}_{\text{i,trace}})_{\text{part obs.} \rightarrow \text{theory}} = \text{PSD}(\delta \mathbf{B}_\perp)_{\text{obs.}}$$
$$\cdot \left(\frac{|\delta \mathbf{V}_{\text{i,trace}}|^2}{|\delta \mathbf{B}_\perp|^2} \right)_{\text{KAW-theory}}, \quad (1c)$$

$$\text{PSD}(\delta \mathbf{V}_{\text{e,trace}})_{\text{part obs.} \rightarrow \text{theory}} = \text{PSD}(\delta \mathbf{B}_\perp)_{\text{obs.}}$$
$$\cdot \left(\frac{|\delta \mathbf{V}_{\text{e,trace}}|^2}{|\delta \mathbf{B}_\perp|^2} \right)_{\text{KAW-theory}}, \quad (1d)$$

$$\text{PSD}\left(\frac{\delta n_e}{n_0} \right)_{\text{part obs.} \rightarrow \text{theory}} = \text{PSD}(\delta \mathbf{B}_\perp)_{\text{obs.}}$$
$$\cdot \left(\frac{|\delta n_e/n_0|^2}{|\delta \mathbf{B}_\perp|^2} \right)_{\text{KAW-theory}}, \quad (1e)$$
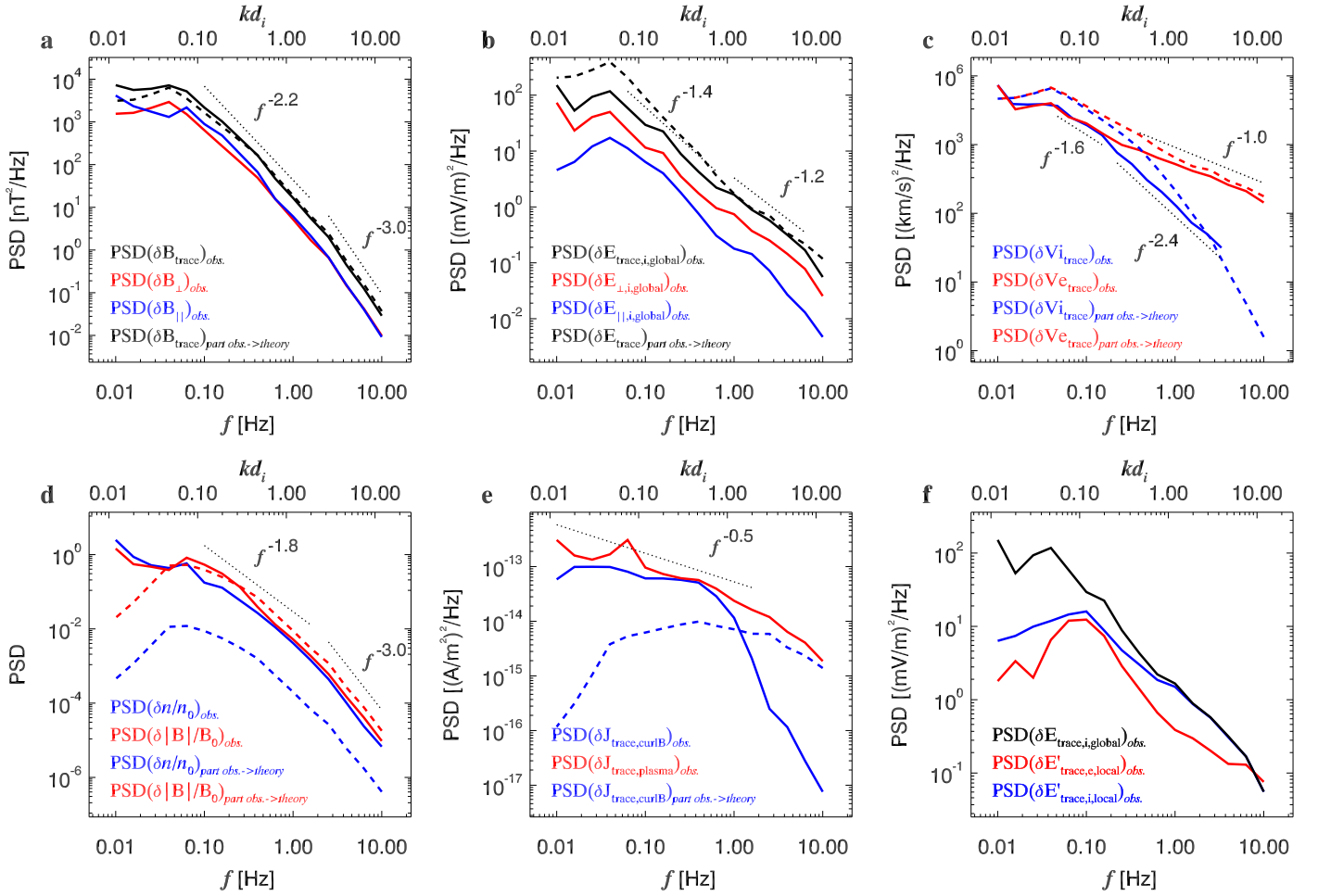
Figure 4. Power spectral densities (PSDs) of a set of variables. Note that the parallel and perpendicular directions for ($\delta B_\parallel$, $\delta B_\perp$, $\delta E_\parallel$, $\delta E_\perp$) refer to the scale-dependent local mean magnetic field coordinate system. (a) PSD($\delta \boldsymbol{B}_{\text{trace}}$)$_{\text{obs.}}$, PSD($\delta B_\perp$)$_{\text{obs.}}$, PSD($\delta B_\parallel$)$_{\text{obs.}}$, and PSD($\delta \boldsymbol{B}_{\text{trace}}$)$_{\text{part obs.}\rightarrow\text{theory}}$ are represented with black solid, red solid, blue solid, and black dashed lines. The segmented power-law spectral profiles are plotted with black dotted lines as a reference. (b) PSD($\delta E_{\text{trace,i,global}}$)$_{\text{obs.}}$, PSD($\delta E_{\perp,\text{i,global}}$)$_{\text{obs.}}$, PSD($\delta E_{\parallel,\text{i,global}}$)$_{\text{obs.}}$, and PSD($\delta E_{\text{trace,i,global}}$)$_{\text{part obs.}\rightarrow\text{theory}}$ are displayed with black solid, red solid, blue solid, and black dashed lines. (c) PSD($\delta \boldsymbol{V}_{\text{i,trace}}$)$_{\text{obs.}}$, PSD($\delta \boldsymbol{V}_{\text{e,trace}}$)$_{\text{obs.}}$, PSD($\delta \boldsymbol{V}_{\text{i,trace}}$)$_{\text{part obs.}\rightarrow\text{theory}}$, and PSD($\delta \boldsymbol{V}_{\text{e,trace}}$)$_{\text{part obs.}\rightarrow\text{theory}}$ are displayed with blue solid, red solid, blue dashed, and red dashed lines, respectively. (d) The blue solid, red solid, blue dashed, red dashed lines are used to represent PSD$\left(\frac{\delta N_e}{N_0}\right)_{\text{obs.}}$, PSD$\left(\frac{\delta |\boldsymbol{B}|}{B_0}\right)_{\text{obs.}}$, PSD$\left(\frac{\delta N_e}{N_0}\right)_{\text{part obs.}\rightarrow\text{theory}}$, and PSD$\left(\frac{\delta |\boldsymbol{B}|}{B_0}\right)_{\text{part obs.}\rightarrow\text{theory}}$, respectively. (e) PSD($\delta J_{\text{trace,CurlB}}$)$_{\text{obs.}}$, PSD($\delta J_{\text{trace,plasma}}$)$_{\text{obs.}}$, and PSD($\delta J_{\text{trace}}$)$_{\text{part obs.}\rightarrow\text{theory}}$ are denoted with blue solid, red solid, and red dashed lines, respectively. (f) PSD($\delta E_{\text{trace,i,global}}$)$_{\text{obs.}}$, PSD($\delta E'_{\text{trace,i,local}}$)$_{\text{obs.}}$, and PSD($\delta E'_{\text{trace,e,local}}$)$_{\text{obs.}}$ are denoted with black solid, blue solid, and red solid lines, respectively.

$$\text{PSD}\left(\frac{\delta |\boldsymbol{B}|}{B_0}\right)_{\text{part obs.}\rightarrow\text{theory}} = \text{PSD}(\delta B_\perp)_{\text{obs.}}$$

$$\cdot \left(\frac{|\delta |\boldsymbol{B}|/B_0|^2}{|\delta \boldsymbol{B}_\perp|^2}\right)_{\text{KAW-theory}}, \quad (1\text{f})$$

$$\text{PSD}(\delta \boldsymbol{J}_{\text{trace}})_{\text{part obs.}\rightarrow\text{theory}} = \text{PSD}(\delta B_\perp)_{\text{obs.}}$$

$$\cdot \left(\frac{|\delta \boldsymbol{J}_{\text{trace}}|^2}{|\delta \boldsymbol{B}_\perp|^2}\right)_{\text{KAW-theory}}. \quad (1\text{g})$$

The PSDs$_{\text{part obs.}\rightarrow\text{theory}}$ are plotted as dashed lines of various colors for comparison with the solid lines of the same colors in the panels of Figure 4. It can be seen in Figure 4(a) that the profile of PSD($\delta \boldsymbol{B}_{\text{trace}}$)$_{\text{part obs.}\rightarrow\text{theory}}$ is almost the same as its counterpart

from pure observation. PSD($\delta \boldsymbol{E}_{\text{trace}}$)$_{\text{part obs.}\rightarrow\text{theory}}$ follows a trend similar to that of PSD($\delta \boldsymbol{E}_{\text{trace,global}}$)$_{\text{obs.}}$. Like in the observations, PSD($\delta \boldsymbol{V}_{\text{i,trace}}$)$_{\text{part obs.}\rightarrow\text{theory}}$ and PSD($\delta \boldsymbol{V}_{\text{e,trace}}$)$_{\text{part obs.}\rightarrow\text{theory}}$ bifurcate from each other at $kd_i \sim 0.2$. Beyond the first break scale, PSD($\delta |\boldsymbol{B}|/B_0$)$_{\text{part obs.}\rightarrow\text{theory}}$ agrees with its observational counterpart. Different from the observed PSD($\delta N_e/N_0$)$_{\text{obs.}}$, PSD($\delta N_e/N_0$)$_{\text{part obs.}\rightarrow\text{theory}}$ is smaller at least by an order of magnitude. This means that the predicted KAW density compressions cannot fully account for the observed density compressions. This observation suggests that the compressive fluctuations consist of contributions from other modes, e.g., the quasi-perpendicular kinetic slow wave (KSW; Hao et al. 2018). The theoretical difference between KSWs and KAWs in terms of Alfvén ratio has been adopted to distinguish these two compressive wave modes at ion scales in the magnetosheath turbulence by Roberts et al. (2018). PSD($\delta \boldsymbol{J}_{\text{trace}}$)$_{\text{part obs.}\rightarrow\text{theory}}$
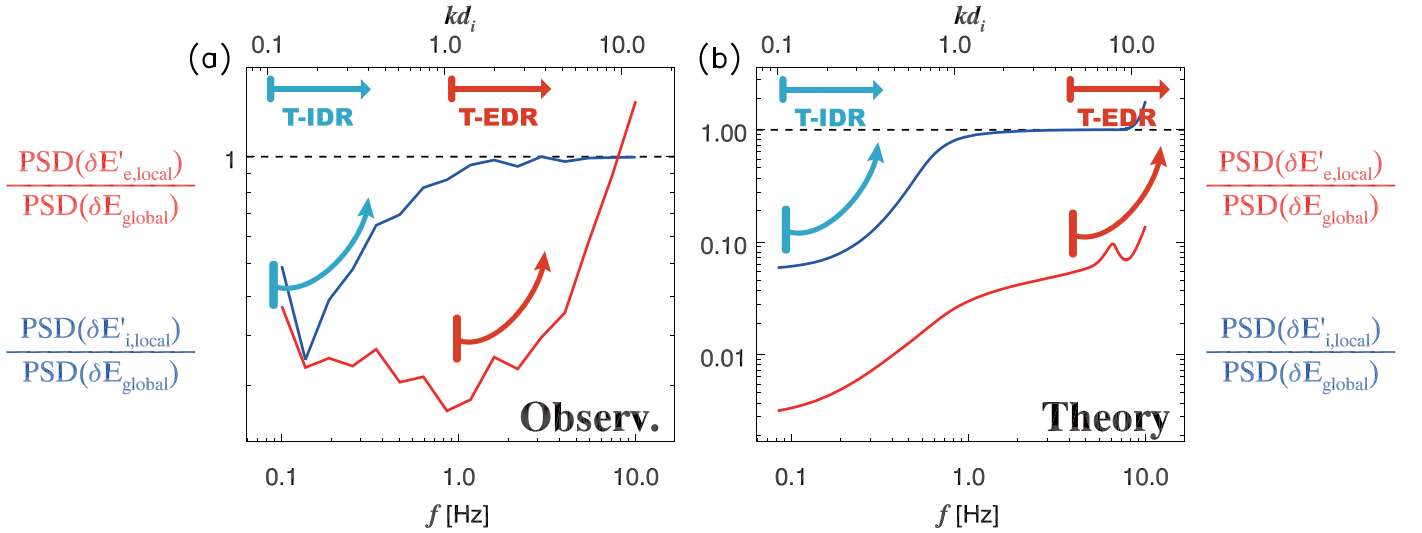
Figure 5. Scale (frequency and wavenumber) profiles of PSD($\delta E'_{e,local}$)/PSD(δE_{global}) (red) and PSD($\delta E'_{i,local}$)/PSD(δE_{global}) (blue) as calculated from observations (left) and from linear kinetic theory (right).

approaches PSD(δJ_{trace})$_{obs.}$ with increasing f_{sc} and kd_i; however, the bias between them at lower f_{sc} remains a mystery to be investigated in the future.

Our method of comparing power spectra of different plasma variables between observations and theoretical predictions for given wave modes is a general and successfully established tool to diagnose the underlying wave nature of the observed fluctuations. In addition to our comparison with kinetic Alfvén waves, this method also enables the identification of other wave modes (e.g., quasi-parallel ion-cyclotron waves, quasi-parallel and quasi-perpendicular whistler waves, oblique mirror modes, and ion acoustic waves) by comparison with observations. In our case, the comparable PSD profiles of $\delta B_\parallel$ and $\delta B_\perp$ indicate that ion-cyclotron waves, quasi-parallel whistler waves or quasi-perpendicular whistler waves are not the dominant wave modes here, as long as our fundamental assumption of the existence of a dominant wave mode is valid. The lack of anisotropy in the ion temperature suggests that it is unlikely that the mirror mode is excited and grows in this case.

5. Diffusion-measure Spectra of Kinetic Alfvénic and Compressible Turbulence

As introduced in our previous work (Duan et al. 2018), the diffusion of magnetic flux relative to the flow of plasma species becomes significant with the contour level of $|\delta E'(k_\parallel, k_\perp)|/|\delta E(k_\parallel, k_\perp)|$ becoming larger than 0 when approaching kinetic scales. This is an application of $|\delta E'|/|\delta E|$, which had been studied in real space to identify the ion and electron diffusion regions related with magnetic reconnection (Hesse et al. 1999). In Figure 5, we calculate and plot the quantities PSD($\delta E'_{e,local}$)/PSD(δE_{global}) and PSD($\delta E'_{i,local}$)/PSD(δE_{global}) as functions of frequency in the SC reference frame. PSD($\delta E'_{i,local}$)/PSD(δE_{global}) rises from 0.1 at $kd_i \sim 0.1$ ($\lambda \sim 63\, d_i$), and gradually saturates on a ratio approaching the asymptotic state of 1 beyond $kd_i \sim 1.0$ ($\lambda \sim 6.3\, d_i$). In comparison, PSD($\delta E'_{e,local}$)/PSD(δE_{global}) stays near 0.1 until $kd_i \sim 1.0$ ($kd_e \sim 0.023$, $\lambda \sim 270\, d_e$), and then rises rapidly beyond $kd_i \sim 1.0$.

The excess portion of PSD($\delta E'_{e,local}$)/PSD(δE_{global}) greater than 1 may not be real: the PSD($\delta E'_{e,local}$) at higher frequency shows a profile with a flat part (see Figure 4(f)), which may be inaccurate and responsible for such an artificial excess phenomenon. The scales where the rapid risings of PSD($\delta E'_{i,local}$)/PSD(δE_{global}) and PSD($\delta E'_{e,local}$)/PSD(δE_{global}) begin can be defined as the outer scales of the turbulence ion diffusion range (T-IDR) and turbulence electron diffusion range (T-EDR) in the wavenumber domain ($\lambda_{outer,T\text{-}IDR} \sim 63\, d_i$, $\lambda_{outer,T\text{-}EDR} \sim 270\, d_e$), respectively.

As a comparison to the observations, the PSD ratios derived from the linear kinetic theory via the "NHDS" code (Verscharen et al. 2016; Verscharen & Chandran 2018) are displayed in Figure 5(b). The trend of PSD($\delta E'_{i,local}$)/PSD(δE_{global}) shows a transition from 0.1 to 1 between $kd_i \sim 0.1$ and $kd_i \sim 1.0$. PSD($\delta E'_{e,local}$)/PSD(δE_{global}) is smaller than PSD($\delta E'_{e,local}$)/PSD(δE_{global}) by an order of magnitude. Throughout the range of scale ($kd_i \in [0.1, 10.0]$, $f_{SC} \in [0.1, 10.0]$ Hz), PSD($\delta E'_{e,loc}$)/PSD(δE_{SC}) almost stays below 0.1, which means that the main contribution to the electric field comes from the Hall term ($-\, V_e \times B$). So the T-EDR for the KAWs based on linear plasma theory must be shorter than $\lambda \sim 27\, d_e$, which corresponds to $kd_i \sim 10.0$. Comparing observation and theory, the scale of commencement for the T-IDR appears to be similar to $\lambda_{T\text{-}IDR} \in [6.3, 63]\, d_i$, while the T-EDR is much larger in observed kinetic turbulence ($\lambda_{T\text{-}EDR,obs} \in [27, 270]\, d_e$) than in theoretical linear kinetic waves ($\lambda_{T\text{-}EDR,theory} < 27\, d_e$).

6. Dissipation Rate Spectra of Kinetic Alfvénic and Compressible Turbulence

Usually, the diffusion effect accompanies dispersion or/and dissipation. In this section, we study the dissipation rate spectra as functions of scale. We invoke the following formulas to estimate the spectrum of the energy conversion rate (ε_{ECR}) and
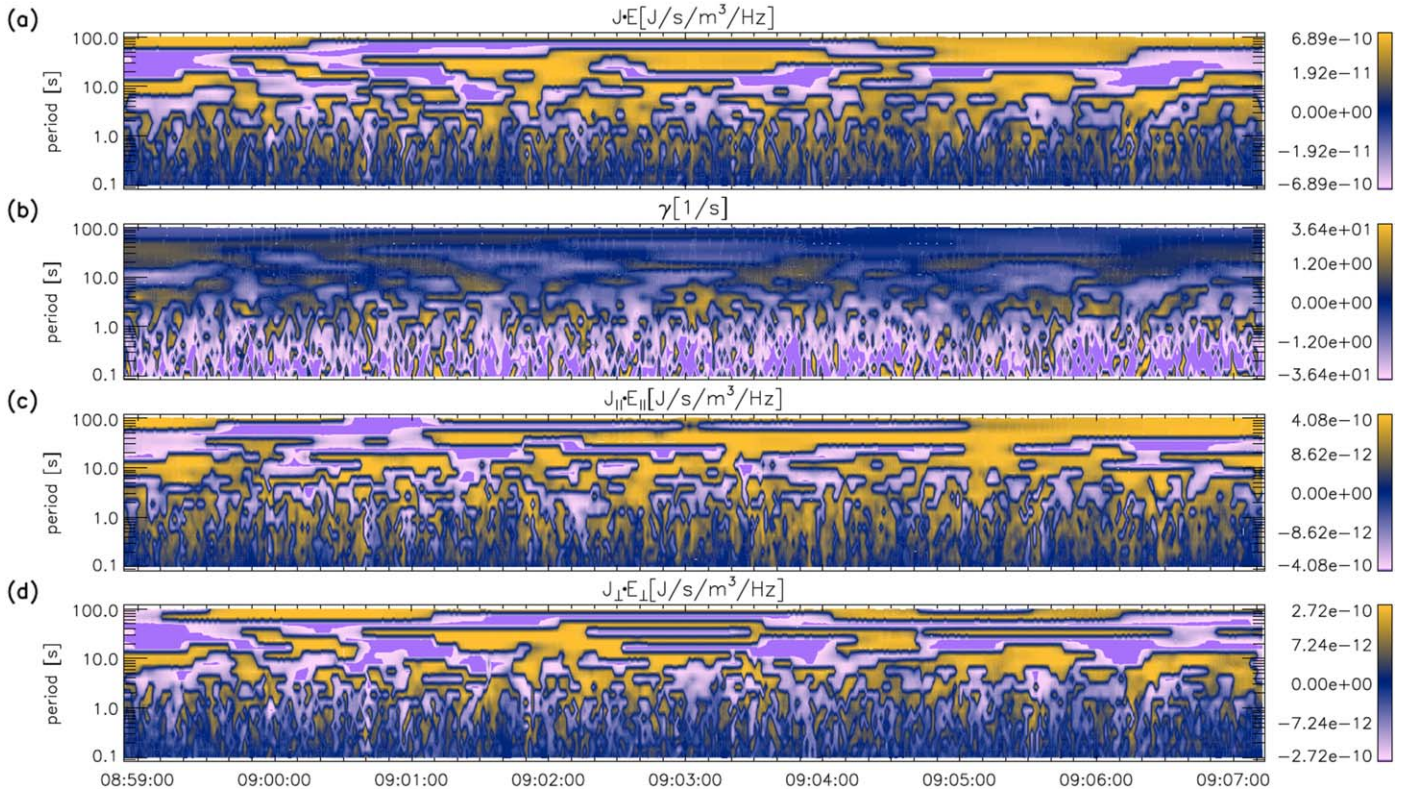
Figure 6. Time–period spectra of local energy conversion rates $\varepsilon_{\mathrm{ECR}}(t, p)$ in all directions (a), in the parallel direction (c), and in the perpendicular direction (d). The normalized local energy conversion rate spectrum (called pseudo-damping rate spectrum) ($\gamma(t, p)$) is displayed in panel (b).

the local pseudo-damping rate (γ),

$$\varepsilon_{\mathrm{ECR}} = \frac{1}{4}(\delta \widetilde{\boldsymbol{J}} \cdot \delta \widetilde{\boldsymbol{E}}^* + \delta \widetilde{\boldsymbol{J}}^* \cdot \delta \widetilde{\boldsymbol{E}}), \qquad (2)$$

$$\gamma = \frac{1}{2} \frac{-1/4(\delta \widetilde{\boldsymbol{J}} \cdot \delta \widetilde{\boldsymbol{E}}^* + \delta \widetilde{\boldsymbol{J}}^* \cdot \delta \widetilde{\boldsymbol{E}})}{|\delta \widetilde{\boldsymbol{B}}|^2/2\mu_0 + \varepsilon_0\,|\delta \widetilde{\boldsymbol{E}}|^2/2}, \qquad (3)$$

where $\delta \widetilde{\boldsymbol{J}}$, $\delta \widetilde{\boldsymbol{J}}^*$, $\delta \widetilde{\boldsymbol{E}}$, and $\delta \widetilde{\boldsymbol{E}}^*$ represent the wavelet spectra and conjugate counterparts of $\boldsymbol{J}$ and $\boldsymbol{E}_{\mathrm{i\text{-}global}}(=\boldsymbol{E}_{\langle V_i \rangle})$, respectively. This technique of calculating dissipation rate spectrum was first introduced and applied to diagnose the dissipation of ion cyclotron waves by He et al. (2019a). The time–period (t–p) diagrams of $\varepsilon_{\mathrm{ECR}}(t, p)$ and $\gamma(t, p)$ are displayed in Figures 6(a) and (b). There is a transition from the alternation between positive and negative values for $\varepsilon_{\mathrm{ECR}}(t, p)$ and $\gamma(t, p)$ at $p > 1$ s to a dominance (prevalence) of positive $\varepsilon_{\mathrm{ECR}}(t, p)$ and negative $\gamma(t, p)$ at $p < 1$ s. Such patterns of $\varepsilon_{\mathrm{ECR}}(t, p)$ and $\gamma(t, p)$ indicate a significant net and time-averaged conversion of energy from fields to particles, suggesting the dissipation of turbulence at the time of observation. We separate the energy conversion from fields to particles into its parallel and perpendicular parts:

$$\varepsilon_{\mathrm{ECR}} = \varepsilon_{\mathrm{ECR},\parallel} + \varepsilon_{\mathrm{ECR},\perp}, \qquad (4)$$

$$\varepsilon_{\mathrm{ECR},\parallel} = \frac{1}{4}(\delta \widetilde{\boldsymbol{J}}_\parallel \cdot \delta \widetilde{\boldsymbol{E}}_\parallel^* + \delta \widetilde{\boldsymbol{J}}_\parallel^* \cdot \delta \widetilde{\boldsymbol{E}}_\parallel), \qquad (5)$$

$$\varepsilon_{\mathrm{ECR},\perp} = \frac{1}{4}(\delta \widetilde{\boldsymbol{J}}_\perp \cdot \delta \widetilde{\boldsymbol{E}}_\perp^* + \delta \widetilde{\boldsymbol{J}}_\perp^* \cdot \delta \widetilde{\boldsymbol{E}}_\perp). \qquad (6)$$

Comparing $\varepsilon_{\mathrm{ECR},\parallel}$ in Figure 6(c) and $\varepsilon_{\mathrm{ECR},\perp}$ in Figure 6(d), we see that $\varepsilon_{\mathrm{ECR},\parallel}$ is prevalently positive at $p < 1$ s, while $\varepsilon_{\mathrm{ECR},\perp}$

still alternates between positive and negative values at $p < 1$ s. This means that the dissipated energy of turbulence is converted directly to the particles in the parallel direction. We note, however, that there may be a transfer of the particles' energy between parallel and perpendicular degrees of freedom via the Lorentz force by magnetic field fluctuations afterward.

The asymmetric or symmetric alternations of $\varepsilon_{\mathrm{ECR}}$, $\varepsilon_{\mathrm{ECR},\parallel}$, and $\varepsilon_{\mathrm{ECR},\perp}$ between negative and positive values in the time sequences result in asymmetric or symmetric probability distribution functions (PDFs) of these variables. Figure 7 illustrates the PDFs of $\varepsilon_{\mathrm{ECR}}$, $\varepsilon_{\mathrm{ECR},\parallel}$, and $\varepsilon_{\mathrm{ECR},\perp}$ on a symmetric logarithmic scale, which are stacked from bottom to top with increasing period. All three PDF($\lg_{\mathrm{sym}}(\varepsilon_{\mathrm{ECR}})$) show a clear V-shape. A remarkable asymmetric pattern is located in the lower segments ($p < 1$ s) of PDF($\lg_{\mathrm{sym}}(\varepsilon_{\mathrm{ECR,trace}})$) and PDF($\lg_{\mathrm{sym}}(\varepsilon_{\mathrm{ECR},\parallel})$), where the PDF on the right side (i.e., at $\varepsilon_{\mathrm{ECR}} > 0$) is greater than its counterpart on the left side. Furthermore, the range of $\varepsilon_{\mathrm{ECR},\parallel}$ on the axis in Figure 7(b) is larger than that of $\varepsilon_{\mathrm{ECR},\perp}$ on the axis in Figure 7(c), meaning that $\varepsilon_{\mathrm{ECR},\parallel}$ is greater than $\varepsilon_{\mathrm{ECR},\perp}$.

According to Equation (3), the negative of the global-averaged damping/growth rate ($\langle -\gamma \rangle_{\mathrm{global}}$) can be estimated as half of the ratio between the global-averaged wavelet spectra of $\frac{1}{4}(\delta \widetilde{\boldsymbol{J}} \cdot \delta \widetilde{\boldsymbol{E}}^* + \delta \widetilde{\boldsymbol{J}}^* \cdot \delta \widetilde{\boldsymbol{E}})$ and $\frac{1}{2\mu_0} |\delta \widetilde{\boldsymbol{B}}|^2 + \frac{\varepsilon_0}{2} |\delta \widetilde{\boldsymbol{E}}|^2$,

$$\langle -\gamma \rangle_{\mathrm{global}} = \frac{1}{2} \frac{\langle 1/4(\delta \widetilde{\boldsymbol{J}} \cdot \delta \widetilde{\boldsymbol{E}}^* + \delta \widetilde{\boldsymbol{J}}^* \cdot \delta \widetilde{\boldsymbol{E}}) \rangle_{\mathrm{global}}}{\langle |\delta \widetilde{\boldsymbol{B}}|^2/2\mu_0 + \varepsilon_0\,|\delta \widetilde{\boldsymbol{E}}|^2/2 \rangle_{\mathrm{global}}}. \qquad (7)$$

Similar to Equations (5) and (6) we obtain different types of $\langle -\gamma \rangle_{\mathrm{global}}$: $\langle -\gamma \rangle_{\mathrm{global,trace}}$, $\langle -\gamma \rangle_{\mathrm{global},\parallel}$, and $\langle -\gamma \rangle_{\mathrm{global},\perp}$ for the damping/growth rate in all directions, in the parallel direction,
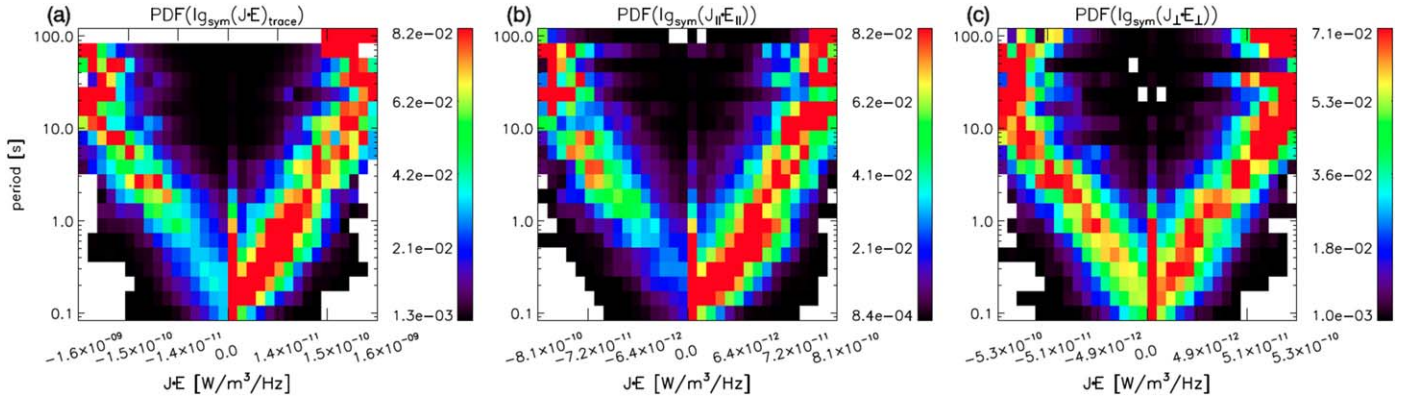
Figure 7. Probability density function of local energy conversion rate (PDF($\lg_{sym}(\varepsilon_{ECR})$)) at various periods in all directions (left), in the parallel direction (middle), and in the perpendicular direction (right). The asymmetry of PDF($\lg_{sym}(\varepsilon_{ECR})$) with a higher level on the right wing appears at periods shorter than 1.0 s and is most evident in the parallel direction.

and in the perpendicular direction, respectively; and $\langle-\gamma\rangle_{global,e,trace}$, $\langle-\gamma\rangle_{global,e,\parallel}$, and $\langle-\gamma\rangle_{global,e,\perp}$ for the damping/growth rates due to electrons in all directions, in the parallel direction, and in the perpendicular direction, respectively. Figure 8(a) shows that $\langle-\gamma\rangle_{global,trace}$ stays zero until $f_{sc} \sim 1$ Hz and rises beyond 1 Hz, a critical frequency in the spacecraft frame corresponding to the critical wavenumber range of $kd_i \in [1, 2]$. Furthermore, $\langle-\gamma\rangle_{global,trace}$ is dominated by $\langle-\gamma\rangle_{global,\parallel}$ rather than $\langle-\gamma\rangle_{global,\perp}$, clearly showing that the turbulence is damped through parallel energization of the plasma. The parallel energization predominantly occurs into the electrons rather than protons, based on the similarity between $\langle-\gamma\rangle_{global,\parallel}$ and $\langle-\gamma\rangle_{global,e,\parallel}$ when comparing the blue lines in Figures 8(a) and (c).

Likewise, the sets of ($-\gamma_{theory,trace}$, $-\gamma_{theory,\parallel}$, $-\gamma_{theory,\perp}$) and ($-\gamma_{theory,e,trace}$, $-\gamma_{theory,e,\parallel}$, $-\gamma_{theory,e,\perp}$) as derived from the linear theory of KAWs under the observed plasma conditions are illustrated in Figures 8(b) and (d). On the one hand, similar to the trend of $\langle-\gamma\rangle_{global,trace}$, $-\gamma_{theory,trace}$ increases from zero around $kd_i \sim 3$, yet to slightly larger values than those for $\langle-\gamma\rangle_{global,trace}$ in the observed turbulence. On the other hand, $-\gamma_{theory,trace}$ is much smaller than $\langle-\gamma\rangle_{global,trace}$ by about two orders of magnitude at $kd_i \sim 10$. Such a difference in magnitude implies some limitations of linear theory when applying it to interpret the measurements. This raises an important question: what physical process is responsible for the remarkable increase of $\langle-\gamma\rangle_{global,trace}$? According to the conservation law of electromagnetic energy (Poynting's theorem),

$$\frac{\partial}{\partial t}\left(\frac{B^2}{2\mu} + \frac{\varepsilon E^2}{2}\right) = -\nabla \cdot \left(\frac{E \times B}{\mu}\right) - J \cdot E, \qquad (8)$$

the divergence of Poynting flux is the first term on the right side of Equation (8). The kinetic energy of the plasma is coupled to the electromagnetic energy, and will be considered in future work. In the previous study by Leamon et al. (1999), the damping rate spectrum was calculated by applying linear kinetic theory to calculate synthetic power spectral density distributions in 3D wavevector space, which are afterward reduced to 1D as a function of frequency in the spacecraft reference frame (see Figures 10 and 11 in their paper). Our method for obtaining the damping rate spectra directly from the

measurements is an extension and continuation of this previous work.

When considering the dynamic equation of the turbulence energy spectrum in both the spatial and wavenumber dimensions, we find

$$\frac{\partial}{\partial t}\left(\frac{|\delta\widetilde{B}(k)|^2}{2\mu} + \frac{\varepsilon|\delta\widetilde{E}(k)|^2}{2}\right) = -\nabla \cdot \left(\frac{\mathrm{Re}(\delta\widetilde{E}(k) \times \delta\widetilde{B}^*(k))}{2\mu}\right)$$
$$- \frac{1}{2}\mathrm{Re}(\delta\widetilde{J}(k) \cdot \delta\widetilde{E}^*(k)) - k\frac{\partial}{\partial k}\varepsilon(k). \qquad (9)$$

Note that Equation (9) already includes some averaging over a few fluctuation periods. The scale-dependent energy conversion spectrum, the second term on the right side of Equation (9), is balanced by three other terms: (1) the time derivative of the generalized electromagnetic energy spectrum, (2) the spatial divergence of the Poynting flux spectrum, and (3) the derivative of the cross-scale transferred energy spectrum in the wavenumber domain. Therefore, one possible cause for the large value of energy conversion may be the convergence of Poynting flux in the magnetosheath turbulence, where the flow together with the Poynting flux is significantly compressed. In addition to the temporal decay of the local turbulence, the extra damped energy may be supplied by the converged Poynting flux. Such an inhomogeneity of the Poynting flux remains after time averaging and does not exist in the linear theory of uniform plasma. The convergence of Poynting flux and its associated influence is beyond the scope of this work and left for future studies.

7. Summary and Discussion

The "3D" (diffusion, dispersion, and dissipation) characteristics of kinetic Alfvénic and compressive turbulence have been investigated in this work by applying newly developed methods to the comparison between the observations from MMS and predictions from kinetic theory. According to our cross-spectral analysis, the turbulence remains mostly Alfvénic from MHD scales down to sub-ion kinetic scales ($kd_i \in [0.01, 10]$). The events of this study are located downstream of the quasi-parallel bow shock, where the plasma parameters are not favorable for the excitation of electromagnetic ion cyclotron or
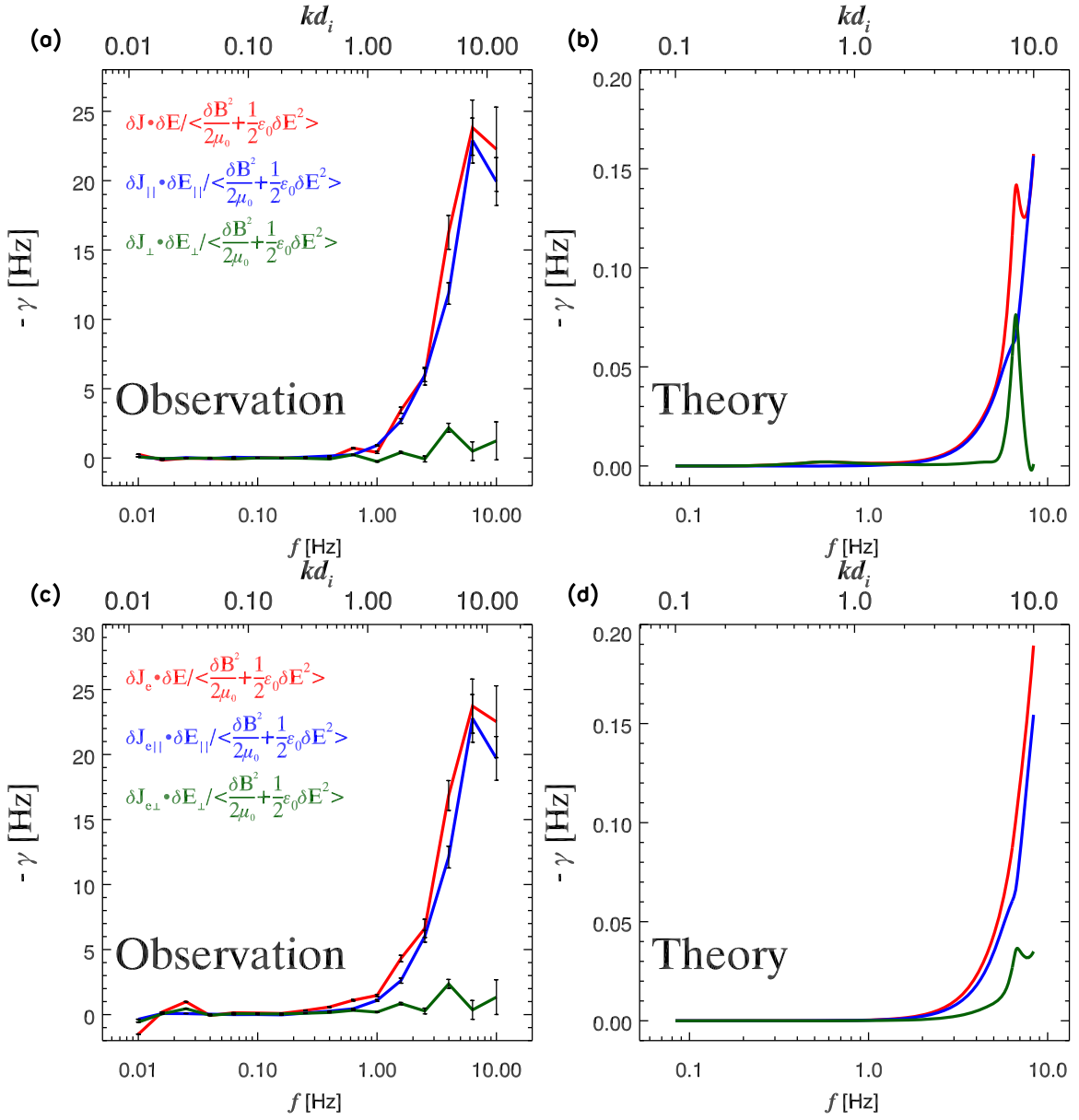
Figure 8. Scale-dependent dissipation rate spectra obtained from observations (left) and predicted from linear theory for KAWs (right). The current densities used to calculate the energy dissipation have contributions from the motion of two species (ions and electrons) (top) and only one species (electrons) (bottom). The dissipation rate spectra in all directions, the parallel direction, and the perpendicular direction are plotted in red, blue, and green. The error bars represent the propagated error of the standard errors of the mean values in the numerator and denominator. The mean values of $\varepsilon_{\mathrm{ECR}}$ and $\frac{1}{2\mu_0}|\delta\widetilde{\boldsymbol{B}}|^2 + \frac{\varepsilon_0}{2}|\delta\widetilde{\boldsymbol{E}}|^2$ are calculated by applying the bootstrapping method to the analyzed time–period spectra of the corresponding quantities.

mirror mode waves. We checked the electromagnetic polarization information and did not find any signatures of quasi-monochromatic ion cyclotron waves or mirror mode waves. This result is supported by our analyses of cross-correlations and power spectral densities, as shown in Figures 2–4, which confirm the existence of kinetic Alfvenic waves. Meanwhile, the turbulence is also compressive throughout this range of scales, with a dominant anticorrelation between N_e and $|\boldsymbol{B}|$ beyond $kd_i \sim 1$. Moreover, the turbulence of this particular interval shows signatures of counter-propagating KAWs. We note that the fluctuation features of the complex magnetosheath turbulence usually vary from region to region. This phenomenon is corroborated by evidence for the agreement of the observed fluctuating quantities with theoretical predictions for KAWs with $\boldsymbol{k} \cdot \boldsymbol{B} > 0$ and $\boldsymbol{k} \cdot \boldsymbol{B} < 0$, respectively. The

counter-propagating KAWs are likely to interact nonlinearly with each other, leading to the cascade of energy in the kinetic regime beyond $kd_i \sim 1$.

The PSD profiles of the quantities ($\delta\boldsymbol{B}$, $\delta\boldsymbol{E}$, $\delta\boldsymbol{V}_e$, $\delta\boldsymbol{V}_i$, δN_e, and $\delta\boldsymbol{J}$) show distinctive and comprehensive features of the segmented power-law spectra of kinetic compressive turbulence. The scale dependence of compressibility in terms of number density and magnetic field strength is characterized through $\mathrm{PSD}(\delta N_e/N_{e0}) \sim \mathrm{PSD}(\delta|\boldsymbol{B}|/B_0)$, $\mathrm{PSD}(\delta B_\parallel) \sim \mathrm{PSD}(\delta B_\perp)$, all of which display a steeper spectral profile ($\sim f^{-3}$) at $f > 1$ Hz after the spectral profile of $\sim f^{-2}$ at $f < 1$ Hz. The dispersive nature of the kinetic compressive turbulence is caused by the Hall effect as well as the inhomogeneous-thermal-pressure effect, which manifest as a flattening of $\mathrm{PSD}(\delta\boldsymbol{E}_{i,\mathrm{global}})$ at $f > 1$ Hz. The Hall effect is caused by the decoupling of motions between electrons

and ions, as evidenced through the bifurcation between $\mathrm{PSD}(\delta V_{\mathrm{e,trace}})_{\mathrm{obs.}}$ $(\sim f^{-1.0})$ and $\mathrm{PSD}(\delta V_{\mathrm{i,trace}})_{\mathrm{obs.}}$ $(\sim f^{-2.4})$ at $f > 0.2$ Hz. Ions become gradually motionless as scale decreases down to electron kinetic scales. They are no longer frozen-in and diffuse relative to the magnetic field.

Motivated by the identification method of ion and electron diffusion regions (IDRs and EDRs) associated with magnetic reconnection with regions of non-zero $E'_{\mathrm{i,local}}$ and $E'_{\mathrm{e,local}}$ as the critical criteria, we use $\mathrm{PSD}(\delta E'_{\mathrm{i,local}})/\mathrm{PSD}(\delta E_{\mathrm{global}})$ and $\mathrm{PSD}(\delta E'_{\mathrm{e,local}})/\mathrm{PSD}(\delta E_{\mathrm{global}})$ to measure the ion and electron diffusion effects in kinetic turbulence. According to the scale dependence of electric field spectral ratio profiles, we identify upper limits on the size of the turbulence ion and electron diffusion ranges (T-IDR and T-EDR) in the wavenumber domain: $k_{\mathrm{T\text{-}IDR}}d_{\mathrm{i}} \sim 0.2$ and $\lambda_{\mathrm{T\text{-}IDR}} \sim 30d_{\mathrm{i}}$ for T-IDR; $k_{\mathrm{T\text{-}EDR}}d_{\mathrm{i}} \sim 2.0$ and $\lambda_{\mathrm{T\text{-}EDR}} \sim 3d_{\mathrm{i}} \sim 130d_{\mathrm{e}}$ for T-EDR. The values of the two outer scales for T-IDR and T-EDR are approximately of the same order as the length scales for magnetic reconnection, which are usually longer than their associated width in reconnecting thin current sheets. The anisotropy of the T-IDR and T-EDR in wavenumber space ($k_{\parallel}$, $k_{\perp}$) for kinetic turbulence is another interesting issue that remains to be explored in the future.

The kinetic Alfvénic and compressive turbulence is found to undergo strong dissipation by converting its electromagnetic field energy to heat the plasma particles, especially the electron species in the parallel direction. This heating also leads to frequent enhancements of T_{e} with $T_{\mathrm{e}\parallel} > T_{\mathrm{e}\perp}$. This observational result conforms with the recent numerical modeling prediction that the electron heating rate dominates over the ion heating rate when ions are hotter than electrons (Parashar & Gary 2019). When both ions and electrons have low plasma β, e.g., young solar wind as measured by Parker Solar Probe at its perihelion, the highly oblique kinetic Alfvén waves may also experience ion-cyclotron resonance and hence heat ions perpendicularly (Isenberg & Vasquez 2019). As seen in the spectral profile of the normalized dissipation rate, the dissipation sets in at $kd_{\mathrm{i}} \sim 1$, and increases in strength with decreasing scales. In the compressed magnetosheath plasma, the dissipated energy may not only come from local turbulence but also the consumption of accumulated Poynting flux. The influence of Poynting flux convergence on the turbulence dissipation and energy conversion is beyond the scope of this study and left as an open question for future study. The kinetic behavior of ions and electrons in phase space associated with kinetic turbulence is another important issue (Zhao et al. 2019a) worthy of in-depth study in the future. To further study the anisotropy of dispersion and diffusion in 3D wavevector space in the future, it would be worthwhile to reconstruct the power spectral density of different variables (e.g., δE and δB) as well as the distributions of their ratios in (ω, $\boldsymbol{k}$) space by employing the k-filtering approach. This method, in general, enables the distinction of various wave modes, if present (propagating in quasi-parallel or quasi-perpendicular directions, occupying major or minor power proportions) in the complex magnetosheath turbulence. A preliminary attempt to quantify the energy partition between different wave modes was conducted by Zhu et al. (2019). This approach successfully decomposes the observed energy spectra of $\delta E_{\parallel}$, $\delta E_{\perp}$, $\delta B_{\parallel}$, and $\delta B_{\perp}$ into contributions from three different wave modes (quasi-perpendicular KAWs, quasi-parallel whistler waves, and quasi-parallel ion acoustic waves), based on a comparison of theoretical and observed transport ratios (polarization) between fluctuating variables.

The coherent structures in strong turbulence, e.g., Alfvénic vortex structures, can also contribute significantly to the energy dissipation and produce plasma heating. Within Alfvénic vortex structures, ion and electron temperatures are roughly correlated with the parallel current density and the parallel vorticity, respectively (Wang et al. 2019). This work mainly focused on the role of the turbulent electric field in energizing the particle species while neglecting the modulation effect by the magnetic field. As derived and demonstrated by Duan et al. (2020), magnetic field fluctuations can play a key role in the redistribution between the parallel and perpendicular degrees of freedom in the kinetic energy of the particle species.

ORCID iDs

Jiansen He https://orcid.org/0000-0001-8179-417X
Xingyu Zhu https://orcid.org/0000-0002-1541-6397
Daniel Verscharen https://orcid.org/0000-0002-0497-1096
Die Duan https://orcid.org/0000-0002-6300-6800
Jinsong Zhao https://orcid.org/0000-0002-3859-6394
Tieyan Wang https://orcid.org/0000-0003-3072-6139

References

Alexandrova, O., Saur, J., Lacombe, C., et al. 2009, PhRvL, 103, 165003
Bale, S. D., Kellogg, P. J., Mozer, F. S., Horbury, T. S., & Reme, H. 2005, PhRvL, 94, 215002
Birn, J., Drake, J. F., Shay, M. A., et al. 2001, JGR, 106, 3715
Birn, J., & Priest, E. R. (ed.) 2007, Reconnection of Magnetic Fields: Magnetohydrodynamics and Collisionless Theory and Observations (Cambridge: Cambridge Univ. Press)
Bourouaine, S., Alexandrova, O., Marsch, E., & Maksimovic, M. 2012, ApJ, 749, 102
Bruno, R., & Carbone, V. 2013, LRSP, 10, 2
Bruno, R., & Trenchi, L. 2014, ApJL, 787, L24
Burch, J. L., Moore, T. E., Torbert, R. B., & Giles, B. L. 2016a, SSRv, 199, 5
Burch, J. L., Torbert, R. B., Phan, T. D., et al. 2016b, Sci, 352, aaf2939
Cerri, S. S., Califano, F., Jenko, F., Told, D., & Rincon, F. 2016, ApJL, 822, L12
Chandran, B. D., Li, B., Rogers, B. N., Quataert, E., & Germaschewski, K. 2010, ApJ, 720, 503
Chasapis, A., Yang, Y., Matthaeus, W. H., et al. 2018, ApJ, 862, 32
Chen, C. H., & Boldyrev, S. 2017, ApJ, 842, 122
Chen, C. H. K., Boldyrev, S., Xia, Q., & Perez, J. C. 2013, PhRvL, 110, 225002
Chen, C. H. K., Klein, K. G., & Howes, G. G. 2019, NatCo, 10, 740
Chen, C. H. K., Leung, L., Boldyrev, S., Maruca, B. A., & Bale, S. D. 2014a, GeoRL, 41, 8081
Chen, L., Wu, D. J., Zhao, G. Q., Tang, J. F., & Huang, J. 2014b, ApJ, 793, 13
Cranmer, S. R., Asgari-Targhi, M., Miralles, M. P., et al. 2015, RSPTA, 373, 20140148
Cranmer, S. R., & van Ballegooijen, A. A. 2012, ApJ, 754, 92
Deng, X. H., & Matsumoto, H. 2001, Natur, 410, 557
Duan, D., He, J., Pei, Z., et al. 2018, ApJ, 865, 89

Duan, D., He, J., Wu, H., et al. 2020, ApJ, 896, 47
Franci, L., Landi, S., Matteini, L., Verdini, A., & Hellinger, P. 2016, ApJ, 833, 91
Fu, H. S., Cao, J. B., Vaivads, A., et al. 2016, JGRA, 121, 1263
Gary, S. P. 1993, Theory of Space Plasma Microinstabilities (No. 7) (Cambridge: Cambridge Univ. Press)
Hao, Y., Lu, Q., Gao, X., et al. 2018, ApJ, 861, 57
He, J., Duan, D., Wang, T., et al. 2019a, ApJ, 880, 121
He, J., Duan, D., Zhu, X., Yan, L., & Wang, L. 2019b, ScChD, 62, 619
He, J., Pei, Z., Wang, L., et al. 2015a, ApJ, 805, 176
He, J., Tu, C., Marsch, E., et al. 2015b, ApJL, 813, L30
He, J., Tu, C., Marsch, E., Bourouaine, S., & Pei, Z. 2013, ApJ, 773, 72
He, J., Tu, C., Marsch, E., & Yao, S. 2012, ApJL, 745, L8
He, J., Wang, L., Tu, C., Marsch, E., & Zong, Q. 2015c, ApJL, 800, L31
He, J. S., Zong, Q. G., Deng, X. H., et al. 2008, GeoRL, 35, L14104
Hesse, M., Schindler, K., Birn, J., & Kuznetsova, M. 1999, PhPl, 6, 1781
Horbury, T. S., Forman, M., & Oughton, S. 2008, PhRvL, 101, 175005
Howes, G. G., Cowley, S. C., Dorland, W., et al. 2008, JGRA, 113, A05103
Howes, G. G., Klein, K. G., & Li, T. C. 2017, JPlPh, 83, 705830102
Huang, S., Sahraoui, F., Deng, X., et al. 2014, ApJL, 789, L28
Isenberg, P. A., & Vasquez, B. J. 2019, ApJ, 887, 63
Kiyani, K. H., Osman, K. T., & Chapman, S. C. 2015, RSPTA, 373, 20140155
Klein, K. G., Howes, G. G., & TenBarge, J. M. 2017, JPlPh, 83, 535830401
Leamon, R. J., Smith, C. W., Ness, N. F., & Wong, H. K. 1999, JGR, 104, 22331
Li, W., Andre, M., Khotyaintsev, Y. V., et al. 2016, GeoRL, 43, 5635
Lion, S., Alexandrova, O., & Zaslavsky, A. 2016, ApJ, 824, 47
Lu, Q. M., Huang, C., Xie, J. L., et al. 2010, JGRA, 115, A11208
Ma, Z. W., & Bhattacharjee, B. 2001, Hall Magnetohydrodynamic Reconnection: The Geospace Environment Modeling Challenge (New York: Wiley)
Matteini, L., Alexandrova, O., Chen, C. H. K., & Lacombe, C. 2017, MNRAS, 466, 945
Matthaeus, W. H., Wan, M., Servidio, S., et al. 2015, RSPTA, 373, 20140154
Mozer, F. S., Bale, S. D., & Phan, T. D. 2002, PhRvL, 89, 015002
Narita, Y., Gary, S. P., Saito, S., Glassmeier, K. H., & Motschmann, U. 2011, GeoRL, 38, L05101
Narita, Y., Plaschke, F., Nakamura, R., et al. 2016, GeoRL, 43, 4774

Øieroset, M., Phan, T. D., Fujimoto, M., et al. 2001, Natur, 412, 414
Parashar, T. N., & Gary, S. P. 2019, ApJ, 882, 29
Perri, S., Carbone, V., & Veltri, P. 2010, ApJL, 725, L52
Phan, T. D., Eastwood, J. P., Shay, M. A., et al. 2018, Natur, 557, 202
Podesta, J. J. 2009, ApJ, 698, 986
Pollock, C., Moore, T., Jacques, A., et al. 2016, SSRv, 199, 331
Pritchett, P. L. 2001, JGR, 106, 3783
Roberts, O. W., Li, X., & Jeska, L. 2015, ApJ, 802, 2
Roberts, O. W., Toledo-Redondo, S., Perrone, D., et al. 2018, GeoRL, 45, 7974
Šafránková, J., Němeček, Z., Přech, L., & Zastenker, G. N. 2013, PhRvL, 110, 025004
Sahraoui, F., Goldstein, M. L., Belmont, G., Canu, P., & Rezeau, L. 2010, PhRvL, 105, 131101
Sahraoui, F., Goldstein, M. L., Robert, P., & Khotyaintsev, Y. V. 2009, PhRvL, 102, 231102
Salem, C. S., Howes, G. G., Sundkvist, D., et al. 2012, ApJL, 745, L9
Schekochihin, A. A., Cowley, S. C., Dorland, W., et al. 2009, ApJS, 182, 310
Smith, C. W., Vasquez, B. J., & Hollweg, J. V. 2012, ApJ, 745, 8
Stix, T. H. 1992, Waves in Plasmas (New York: Springer)
Tang, B.-B., Li, W. Y., Graham, D. B., et al. 2019, GeoRL, 46, 3024
Torbert, R. B., Russell, C. T., Magnes, W., et al. 2016, SSRv, 199, 105
Tu, C. Y., & Marsch, E. 1995, SSRv, 73, 1
Verscharen, D., Chandran, B. D., Klein, K. G., & Quataert, E. 2016, ApJ, 831, 128
Verscharen, D., & Chandran, B. D. G. 2018, RNAAS, 2, 13
Wang, X., Tu, C. Y., He, J. S., & Wang, L. H. 2018, JGRA, 123, 68
Wang, T., Alexandrova, O., Perrone, D., et al. 2019, ApJL, 871, L22
Woodham, L. D., Wicks, R. T., Verscharen, D., & Owen, C. J. 2018, ApJ, 856, 49
Wu, D. J., Feng, H. Q., Li, B., & He, J. S. 2016, JGRA, 121, 7349
Wu, H., Verscharen, D., Wicks, R. T., et al. 2019, ApJ, 870, 106
Yang, Y., Wan, M., Matthaeus, W. H., et al. 2019, MNRAS, 482, 4933
Zhao, G. Q., Feng, H. Q., Wu, D. J., Pi, G., & Huang, J. 2019a, ApJ, 871, 175
Zhao, J. 2015, PhPl, 22, 042115
Zhao, J., Wang, T., Shi, C., et al. 2019b, ApJ, 883, 185
Zhou, M., Deng, X., Fu, S., et al. 2009, ScChG, 52, 626
Zhu, X., He, J., Verscharen, D., & Zhao, J. 2019, ApJ, 878, 48